Technique for Rapid Mass Determination of Airborne Microparticles Based on Release and Recapture from an Optical Dipole Force Trap

Gehrig Carlse [*], Kevin B. Borsos, Hermina C. Beica, Thomas Vacheresse, Alex Pouliot, Jorge Perez-Garcia, Andrejs Vorozcovs, Boris Barron, Shira Jackson, Louis Marmet, and A. Kumarakrishnan[†]

Department of Physics and Astronomy, York University, Toronto, Ontario M3J 1P3, Canada

We describe a method for the rapid determination of the mass of particles confined in a free-space optical dipole force trap. The technique relies on direct imaging of drop-and-restore experiments without the need for a vacuum environment. In these experiments, the trapping light is rapidly shuttered with an acousto-optic modulator, causing the particle to be released from and subsequently recaptured by the trapping force. The trajectories of both the falls and restorations, imaged using a high-speed CMOS sensor, are combined to determine the particle mass. We corroborate these measurements using an analysis of position autocorrelation functions and the mean-square displacement of the trapped particles. We report a statistical uncertainty of less than 2% for masses on the order of 5×10^{-14} kg using a data acquisition time of approximately 90 s.

I. INTRODUCTION

The development of optical dipole force (ODF) laser traps to confine dielectric particles [1–5] has led to wide-ranging applications across many fields of research. Notable examples include the development of far-off resonance traps for confining atoms [6,7], the use of optical tweezers to generate three-dimensional optical crystals [8,9], and the application of ODF traps for the manipulation of biological molecules [10,11], measurements of bond strengths [12], and protein synthesis [13,14].

The progression of this field has led to powerful experiments investigating the diffusive kinematics of single particles trapped in liquids or free space. The pioneering experiments in Refs. [15–19] have enabled investigation of the timescales on which diffusive Brownian motion transitions to ballistic motion. Other lines of inquiry have focused on particle kinematics to study the properties of the trap itself [20–22], the color of the stochastic force associated with Brownian motion [23], the development of precise force sensors [24], determinations of fluid viscosity [25,26], and measurements of the polarizability of trapped particles [27]. Progress in these areas has focused on improving detection bandwidth [28] and spatial resolution [29] to investigate smaller time and length scales. These experiments have employed complementary techniques, such as analyses of power spectral densities [30,31], and position and velocity autocorrelation functions [15,17].

Recently, there has also been widespread interest in employing optical tweezers to perform precise mass measurements of trapped particles [32–34]. In Table I we show a representative compilation of such tweezer-related measurements. The most sensitive and accurate mass measurement involving optical tweezers has been obtained using underdamped ODF traps operated in a vacuum environment [32]. In Ref. [32], the trapped particle was driven using an alternating electric field and the mass was determined by fitting to the power spectral density (PSD) of the motion. This technique has been successful in characterizing masses on the femtogram scale with a precision of 0.25%. Other examples of mass determinations in the range of 10^{-10}–10^{-15} kg involve photophoretic traps [35] and have achieved precision at the level of a few percent [36,37].

In this paper, we show that the use of video microscopy to track the release and recapture of particles held in a free-space single-beam gradient trap results in a simple technique for the rapid and precise determination of the particle's mass. This technique does not require a vacuum environment or electromechanical feedback systems. Additionally, it is demonstrated here using modest laser powers and a small field of view. The precise timing required for the release and recapture of trapped particles is enabled by amplitude modulation using an acousto-optic modulator. As a result, we combine the advantages of tight confinement in an ODF trap and the capacity to

_____
[*]gehrig.carlse@gmail.com
[†]akumar@yorku.ca

TABLE I. Summary of contemporary tweezer-based mass measurements. The last column indicates the statistical (stat.) and systematic (syst.) uncertainties.

Reference	Technique	Mass (kg)	Stat. and syst. uncertainties
Huang *et al.* (2011) [15][a]	Continuous VACF analysis	1.26×10^{-14}	<10% and <10%
Bera *et al.* (2016) [35][b]	Power spectrum analysis	9.68×10^{-11}	15% (stat. only)
Lin *et al.* (2017) [36][b]	Optically forced modulation	9.00×10^{-13}	2% and 6%
Chen *et al.* (2018) [37][b]	Dynamic power modulation	6.3×10^{-15}	Not estimated
Blakemore *et al.* (2019) [33]	Electrostatic co-levitation	8.40×10^{-15}	1% and 1.8%
Ricci *et al.* (2019) [32][c]	Electrostatically driven resonance	4.01×10^{-18}	0.25% and 0.5%
This work	Drop and restore	5.58×10^{-14}	1.4% and 13%

[a]Solution-based experiment.
[b]Photophoretic trapping experiment.
[c]Experiments in low-pressure vacuum environments.

observe unconstrained particle kinematics sensitively as in the drop-tower studies of Ref. [38]. Building on techniques to study the ballistic expansion of ultracold atomic samples [39], we track the centroid of particles dropped in free space to infer the damping rate and analyze the trajectory of the recaptured particle to determine the particle mass. These measurements are corroborated by separate studies of the position autocorrelation function (PACF) and mean-square displacement (MSD). We show that masses on the order of 10^{-14} kg associated with resinous particles with diameters of a few micrometers can be determined with a statistical precision of about 2% in measurement times of approximately 90 s.

In what follows, we first describe the theoretical framework for particle kinematics and the features of the MSD and PACFs in Sec. II. In Sec. III we outline the experimental setup and in Sec. IV we present the main results of the paper.

II. THEORY

The stochastic motion of a particle in a fluid bath can be modeled by the Langevin equation

$$m\frac{\partial^2 x}{\partial t^2} + \gamma\frac{\partial x}{\partial t} = F(t), \qquad (1)$$

where m is the mass of the particle, γ is the damping coefficient associated with the surrounding medium, and $F(t)$ is the stochastic force that produces Brownian motion [40].

This treatment can be readily modified to include a harmonic potential due to an ODF [41,42]:

$$\frac{\partial^2 x}{\partial t^2} + \Gamma\frac{\partial x}{\partial t} + \frac{\kappa}{m}x = A(t). \qquad (2)$$

Here $\Gamma = \gamma/m$ is the damping rate, κ is the spring constant of the ODF trap, and the stochastic acceleration is represented as $A(t) = F(t)/m$.

Investigations into such stochastic systems have centered upon the study of the PSD of the motion and its Fourier transform, the PACF [17]. The characteristic timescale on which Brownian motion transitions to ballistic motion is defined by $\tau_p = 1/\Gamma = m/\gamma$, known as the momentum relaxation time. Details of the kinematics on timescales much smaller than τ_p have been investigated in Refs. [16,18,19] in both underdamped and overdamped regimes by direct computation of correlation functions. In addition, numerous other experiments have relied on measurements of the PSD to extract physical properties, such as the color of the stochastic force [23], the viscosity of the fluid [25], and the polarizability [27] and mass of particles [32].

For applications based on free-space experiments, it is instructive to quantify the timescale set by τ_p to better understand the details of the particle kinematics. For a spherical particle, Stokes' law for the damping coefficient is given by $\gamma = 6\pi r\eta$, where r is the particle radius and η is the dynamic viscosity of the surrounding medium. The form of Stokes' law results in a momentum relaxation time that scales as r^2. Using the equipartition theorem and the kinetic theory of gases in which colliding particles are treated as hard spheres, it can be shown that the viscosity of a medium is described by $\eta = 1/6r_g^2\sqrt{k_B T m_g/\pi^3}$, where k_B is the Boltzmann constant, T is the temperature, and r_g and m_g are the radius and mass of a gas molecule [43]. For nitrogen gas at $T = 300$ K, the value of η is approximately 17 μPa s, which represents a reasonable estimate for the empirical viscosity of air (18 μPa s) [44]. For a particle of radius 3 μm and mass approximately 10^{-13} kg immersed in air at room temperature, this treatment gives a momentum relaxation time of approximately 100 μs. While our experiments are designed with a temporal resolution comparable to this value of τ_p, our drop-and-restore technique averages over the effects of Brownian motion by repeating the measurements on timescales much larger than τ_p. We corroborate the resulting mass determinations using the calculation of PACFs, a complementary technique that

can probe kinematics occurring on timescales of approximately τ_p.

For a particle in an ODF trap, the PACF and PSD have been calculated for Brownian motion in the overdamped, underdamped, and critically damped regimes by solving Eq. (2) [41,42,45]. The expression for the PACF in the overdamped case, which is of interest here, is given by

$$\langle x(t_0)x(t_0+t)\rangle = \frac{k_B T}{m\omega_0^2}e^{(-\gamma/2m)t}\left[\cosh(bt)+\frac{\gamma}{2mb}\sinh(bt)\right],$$

(3)

where t_0 is an arbitrary time, $b = \frac{1}{2}\sqrt{\Gamma^2 - 4\omega_0^2}$, and $\omega_0 = \sqrt{\kappa/m}$ is the natural angular frequency of the trap.

In highly overdamped cases, where $\Gamma^2 \gg 4\omega_0^2$, it is also possible to further approximate Eq. (2) by omitting the inertial term [46] so that the equation of motion becomes

$$\gamma\frac{\partial x}{\partial t} + \kappa x = F(t),$$

(4)

resulting in the simplified autocorrelation function

$$\langle x(t_0)x(t_0+t)\rangle = \frac{k_B T}{\kappa}e^{-t/\tau_0}$$

(5)

with a well-defined time constant known as the correlation time $\tau_0 = \gamma/\kappa$. Reconstructions of the correlation functions in Eqs. (3) and (5) can be used to corroborate the mass measurements obtained using the drop-and-restore experiments discussed in this paper.

In a stochastic system, the PACF is also directly related to the MSD of the particle, which is given by

$$\langle[\Delta x(t)^2]\rangle = 2[\langle x(t_0)^2\rangle - \langle x(t_0)x(t_0+t)\rangle],$$

(6)

where the first term in the square bracket is the variance of the position and the second term is the PACF [8,47]. The transition from Brownian motion to ballistic motion can be inferred by observing the change in slope of the MSD that occurs on timescales on the order of τ_p [17]. In this paper, we construct the MSD on the basis of Eq. (6) using the PACFs in Eqs. (3) and (5), and use the short timescale behavior to further check the consistency of the mass determinations made using the drop-and-restore and PACF experiments.

In the drop-and-restore experiments, the trapped particle is repeatedly released from the ODF trap. The motion of the particle falling in gravity is modeled by

$$\frac{\partial^2 x}{\partial t^2} + \Gamma\frac{\partial x}{\partial t} - g = A(t),$$

(7)

where $g = -9.8$ m/s^2 is the acceleration due to gravity in this coordinate system. Here, since we average uncorrelated repetitions, the stochastic driving term plays no role

and the resulting solution to Eq. (7) is given by

$$x(t) = \frac{g}{\Gamma}\left[t + \left(\frac{1}{\Gamma}+\frac{v_r}{g}\right)(e^{-\Gamma t}-1)\right],$$

(8)

where v_r represents the initial velocity of the released particle, which should average to zero over many uncorrelated repetitions. Therefore, a fit to the displacement-time graph of a falling particle can be used to extract Γ.

In the subsequent step of this experiment, the laser confinement is turned on so that the particle is restored to the trap center. This behavior is modeled by

$$\frac{\partial^2 x}{\partial t^2} + \Gamma\frac{\partial x}{\partial t} + \omega_0^2 x - g = A(t).$$

(9)

Once again, since numerous uncorrelated restorations are averaged, the stochastic drive does not contribute to the resulting effective solution to Eq. (9), which is given by

$$x(t) = x_0 e^{(-\Gamma/2)t}\left[\cosh(bt)+\frac{\Gamma}{2b}\sinh(bt)\right]$$
$$+ \frac{v_0}{b}[e^{(-\Gamma/2)t}\sinh(bt)],$$

(10)

where x_0 is the initial position and v_0 is the recapture velocity of the particle at the time when the laser force is turned on to restore the particle. Thus, it is possible to infer the value of m from a fit to Eq. (10) using values of Γ from the drop experiments, and κ from independent measurements of the trap spring constant.

We now comment on the expectations for the recapture velocity in Eq. (10), where, for drop times $t \gg \tau_p$, v_0 can be estimated as the sum of the terminal velocity and the effect of the ODF during the first frame of exposure. The variation in the recapture velocity as a function of drop time can be modeled by

$$v_0(t) = v_T - t_{\exp}\kappa x(t)/m,$$

(11)

where $v_T = g/\Gamma$ is the terminal velocity of the particle, $t_{\exp}$ is the exposure time for a single frame of acquisition, and $x(t)$ is the trajectory described by Eq. (8).

III. EXPERIMENTAL DETAILS

The experiments are carried out with a homebuilt laser system, operating at 780 nm, consisting of a master oscillator and semiconductor waveguide TA placed on a pneumatically isolated optical table. A schematic of the experimental setup is shown in Fig. 1. The power stability of the master oscillator has a characteristic Allan deviation of 5×10^{-6} at 10 s [48] and the TA has an output power of approximately 2 W [49]. The output of the TA is fiber coupled and gently focused through an AOM driven at
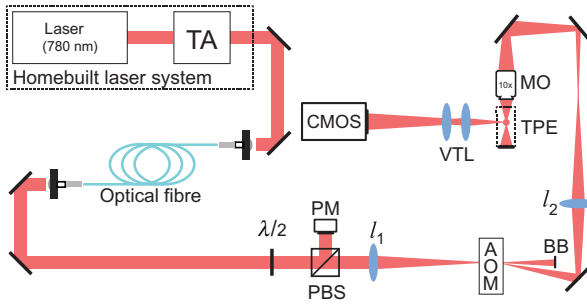
FIG. 1. Schematic diagram of the experimental setup. The focal lengths of the beam shaping lenses are $l_1 \sim 45$ cm and $l_2 \sim 30$ cm. The mirrors in between the acousto-optic modulator (AOM) and the $10\times$ objective (MO) act as a periscope such that the beam entering the MO is directed downward along the vertical direction. Here, TA represents the tapered amplifier, $\lambda/2$ represents a half-wave plate, PBS represents a polarizing cube beam splitter, PM represents a power meter, BB represents a beam block, TPE represents the trapped particle enclosure, VTL represents the variable telescope, and CMOS represents the camera.

80 MHz so that the diffracted beam could be turned off or on in approximately 150 ns. As a result, it is possible to rapidly release the trapped particle in a gravitational field, and subsequently restore the particle to its equilibrium position. The turn on and turn off of the diffracted beam from the AOM is controlled by a pulse generator operated at repetition rates ranging from 0.5–20 Hz. The pulse width that defines the free-fall time of the particle is precise to the level of 1 ns. The maximum power in the diffracted beam (250 mW) is controlled with a waveplate and polarizing cube beam splitter. The diffracted beam is expanded and focused through a $10\times$ microscope objective (NA 0.25) so that the focus of the beam is approximately 5 mm from the end face of the objective lens. The intensity gradients associated with the ODF trap are characterized using a scanning knife edge spatial profiler as shown in Fig. 2(a). The focal region is surrounded by a tightly sealed enclosure with sliding glass windows to reduce air currents. In this free-space configuration, the trapped particles are introduced by ablating from the tip of a permanent marker inserted into the enclosure. We note that this is a simple and effective technique for introducing particles into a free-space optical tweezers setup since the ablated particles have near zero velocity. Other techniques for introducing trapped particles are described in Refs. [2,16,17,20,50,51]. The light scattered from the trapped particle in the transverse direction is imaged onto a CMOS sensor using a simple two-lens telescope with a variable magnification ranging from approximately $40\times$–$80\times$. The CMOS sensor (Phantom UHS-12 v2012) consisted of an 800×1280 pixel array with an overall size of 2.24×3.58 cm^2, which amounts to a pixel size of 28 μm. The camera is operated in continuous mode at a variable frame rate ranging from
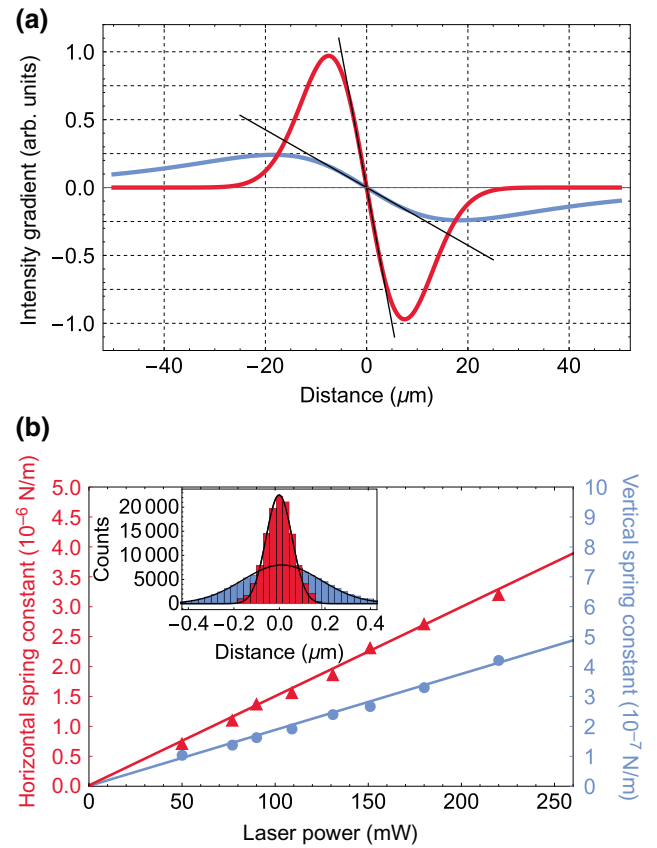

FIG. 2. (a) Intensity gradients along the vertical (light blue) and horizontal (red) directions. The straight lines indicate the linear (harmonic) ranges of the potentials. (b) The spring constant as a function of laser power along the horizontal (left/red axis) and vertical (right/blue axis) directions. The linear fits to the two data sets give $\kappa = [(1.49 \pm 0.04) \times 10^{-8}$ (N/m)/mW]$P + [(1.36 \pm 5.61) \times 10^{-8}]$ N/m along the horizontal direction and $\kappa = [(1.87 \pm 0.07) \times 10^{-9}$ (N/m)/mW]$P + [(1.11 \pm 4.16) \times 10^{-8}]$ N/m, along the vertical, where P is the laser power in milliwatts. Inset shows examples of position histograms in the vertical (light blue bar) and horizontal (red bar) directions for a representative laser power (77.5 mW). The black lines show Gaussian fits whose widths are used to calculate the spring constants.

1×10^4 to 2×10^5 frames per second (frames/s). The imaging system is calibrated by photographing a ruled micrometer slide placed in the object plane of the telescope. The calibration involves fitting the profiles of successive rulings in the image plane to Gaussians and determining their separations in pixel units. Image sequences are stored in on-board memory and transferred to a computer for data processing. For the drop-and-restore experiments, 100 independent image sequences are averaged to improve the signal-to-noise ratio. In contrast, the PACF measurements rely on a continuous record length of images. To compensate for the lack of averaging in the PACF measurements, an intensity filter is used to reduce

the effect of broadband background noise entering the telescope.

IV. RESULTS

A. Spring constant determination

In Fig. 2(b) we show the measurement of the spring constant of the ODF trap as a function of laser power. For each laser power, the spring constant is obtained from a Gaussian fit to the histograms of instantaneous positions [inset in Fig. 2(b)]. The Gaussian fit has a functional form $G(x) = Ce^{-\kappa x^2/k_B T}$, where x is the instantaneous position and C is a normalization constant [52]. Here, the particle positions are recorded with an exposure time of 10 μs on a suitably long timescale ($t \gg \tau_0$) to ensure uncorrelated measurements. This method of determining the trap spring constant is independent of measurements of the damping or the particle mass, contrasting with alternative approaches that rely on the power spectrum. From linear fits in Fig. 2(b), we obtain spring constants of 1.49×10^{-6} N/m in the horizontal direction and 1.87×10^{-7} N/m in the vertical direction for a typical laser power of 100 mW. We note that the offsets predicted by the fit equations in Fig. 2(b), which are small, can be used to estimate the inherent noise in the detection system [53]. We also note that relative values of the spring constants are consistent with the magnitudes of their respective intensity gradients [see Fig. 2(a)].

B. Mass determination from drop-and-restore experiments

In Fig. 3(a) we show the position of the released particles as a function of "drop time" (i.e., the time after release from the trap). The position after each drop time is determined by averaging 100 individual uncorrelated repetitions. This free-fall data is fit to Eq. (8) to determine Γ, with a statistical uncertainty of approximately 1%. Since the system is highly damped, the trajectory is dominated by the linear term in Eq. (8), the slope of which defines v_T.

In Fig. 3(b) we show representative trajectories of particles that are being restored to the equilibrium position of the trap, after various drop times. The overall data collection time for a set of 13 drop-and-restore experiments is approximately 90 s. The restoration trajectories are fit to Eq. (10) on the basis of known values for κ from the calibration [see Fig. 2(b)], as well as Γ and x_0 from the drop experiment [see Fig. 3(a)]. Therefore, we are able to determine the mass of the falling particle from a two-parameter fit involving m and v_0.

In Fig. 4(a) we show the mass extracted from the restoration trajectories for the drop times shown in Fig. 3(a). We find no systematic dependence on the drop time. The error bar represents the statistical uncertainty of the single parameter fit. We report a mass measurement of $5.58 \times$
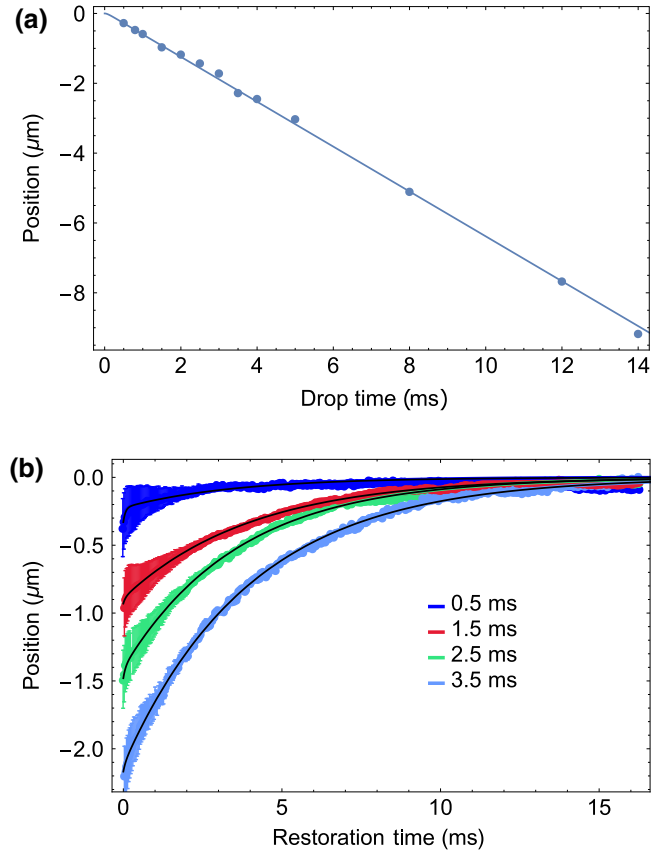

FIG. 3. (a) Shows the fall distance as a function of drop time and a fit to Eq. (8) with $\Gamma = 15.1 \pm 0.1$ kHz and $v_r = 0.7 \pm 0.5$ μm/ms. (b) Shows the restoration trajectories along the vertical axis of the trapping beam for a representative set of drop times. Fits to Eq. (10) are superimposed on the data in black. The spring constant for these restorations is $\kappa = 2.2 \times 10^{-7}$ N/m. The data for both the drop and the restore experiments represent averages of 100 independent repetitions and the error bars indicate the standard deviation of these repetitions. Here, we take the value of g to be -9.80 m/s^2.

10^{-14} kg, with a statistical uncertainty of 1.4%, based on the 13 measurements carried out with $\kappa = 2.2 \times 10^{-7}$ N/m. We estimate the overall uncertainty in m by numerically varying the parameters κ, Γ, and x_0 within experimental error, finding the statistical variation in m from the resulting trajectory fits, and combining these individual uncertainties in quadrature. In this manner, we infer a systematic uncertainty in m of 6×10^{-15} kg (approximately 13%).

To further investigate the effect of trap stiffness, we repeat the drop-and-restore experiments for a subset of drop times, with a significantly larger (approximately $\times 2$) spring constant. We find that these mass measurements are consistent with those obtained with a smaller spring constant, as shown in Fig. 4(a). Specifically, we find a
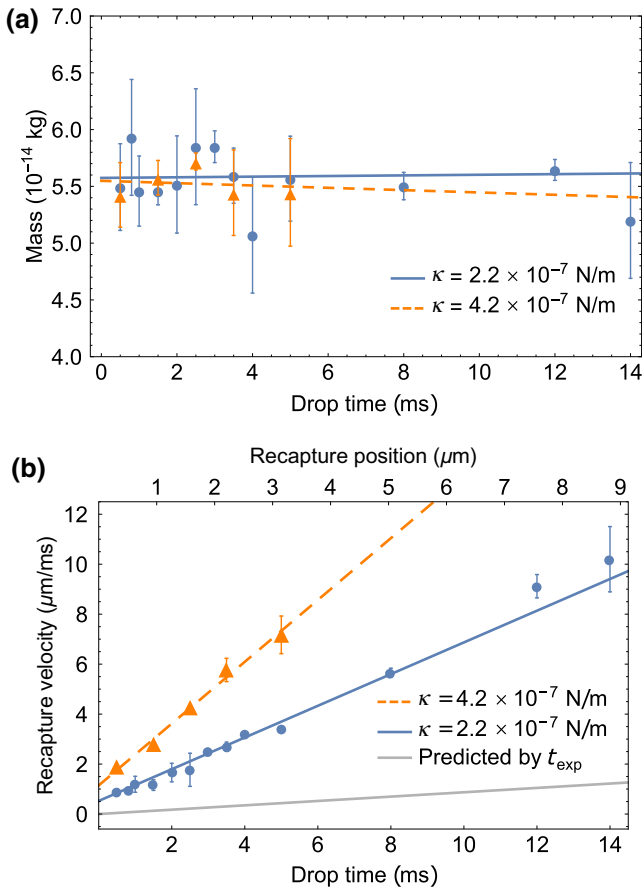
FIG. 4. (a) Mass determined using the drop-and-restore technique for various drop times. The restoration fits are performed using the values $\Gamma = 1.511 \times 10^4$ Hz from the drop experiment and $\kappa = 2.2 \times 10^{-7}$ N/m (circles) and $\kappa = 4.2 \times 10^{-7}$ N/m (triangles) from the vertical spring constant measurements. The fit line for $\kappa = 2.2 \times 10^{-7}$ N/m gives an offset value of $(5.58 \pm 0.08) \times 10^{-14}$ kg and a slope that is consistent with zero as expected, namely, $(2.74 \pm 9.86) \times 10^{-17}$ kg/ms. The fit line for $\kappa = 4.2 \times 10^{-7}$ N/m gives an offset value of $(5.55 \pm 0.12) \times 10^{-14}$ kg and a slope that is also consistent with zero, $(-1.1 \pm 4.0) \times 10^{-16}$ kg/ms. (b) Fit values of v_0 from Eq. (10) as a function of drop time (lower axis) and recapture position with respect to the trap center (upper axis). The two horizontal axes are linearly dependent as described by the drop trajectory in Fig. 3(a). For $\kappa = 2.2 \times 10^{-7}$ N/m (circles), the solid fit line, which models the data as a function of drop time, gives an offset value of $v_0(t = 0) = (0.5 \pm 0.1)$ μm/ms, and an acceleration given by the slope of (0.63 ± 0.03) μm/ms². For $\kappa = 4.2 \times 10^{-7}$ N/m (triangles), the dashed fit line, which models the data as a function of the drop time, gives an offset value of $v_0(t = 0) = (1.2 \pm 0.2)$ μm/ms, and an acceleration given by the slope of (1.28 ± 0.07) μm/ms². The predicted value of the recapture velocity, also as a function of drop time, as defined by Eq. (11), is shown by the light gray trendline.

mass of 5.55×10^{-14} kg, with a similar statistical uncertainty of approximately 2%, and once again, no systematic dependence of the mass on the drop time. This abbreviated

study as a function of spring constant helps to demonstrate the insensitivity of the drop-and-restore technique to changes in the trap stiffness.

In Fig. 4(b) we show the fit values of the recapture velocity v_0, as a function of the drop time and recapture position, for each of the mass determinations shown in Fig. 4(a). The fit lines (dashed and solid) show that the initial recapture velocity continues to increase as the particle is allowed to fall further from the equilibrium position. In Fig. 4(b) we also show the predicted value of the recapture velocity, as defined by Eq. (11) (solid light gray line). We attribute the differences between the two trend lines and the prediction to an impulse proportional to the distance from the trap center imparted by the turn on and turn off of the AOM that produces a transient, uneven illumination of the particle. Our conjecture is supported by the drop experiments shown in Fig. 3(a), where the fit to Eq. (8) yields a small initial velocity. We note that this effect, indicative of a small impulse in the drop data, is consistent with the offset extracted from the fit in Fig. 4(b). We suggest that these features of the data arise because the resultant impulse imparted scales with distance from the beam focus due to the position-dependent nature of the ODF. During the turn off, or during the turn on following a short drop time, the position of the particle is near the uniformly illuminated region around the equilibrium position of the trap. In contrast, when the AOM is turned on after longer drop times, the particle is at increasing distances from the trap center where any uneven and transient illumination due to the AOM will have a larger effect. Therefore, the linear dependence of the recapture velocity on the drop time in Fig. 4(b) can be attributed to the combined effects of the laser force, the impulse from the AOM, and gravity.

We also note that the recapture velocities measured with a higher trap spring constant exhibit a larger slope, as a function of drop time, in comparison to data obtained with a smaller spring constant. This behavior further supports our conjecture that larger recapture velocities arise from the combination of a stronger laser force and the impulse from the AOM.

C. Mass determination from autocorrelation functions

In Fig. 5(a) we show representative examples of PACF-sgenerated from data sets that are several seconds in duration with a frame rate of 10^5 frames/s. This data, obtained at various laser powers, represents the time-domain analog of other techniques for mass determination that rely on the PSD [32,36]. Here, however, the smoothness of the PACF suffers due to the record length, which is restricted to match that of the drop-and-restore experiments. While the PACFs can be fit to Eq. (3), the complex functional form results in an overestimation of the uncertainty in the
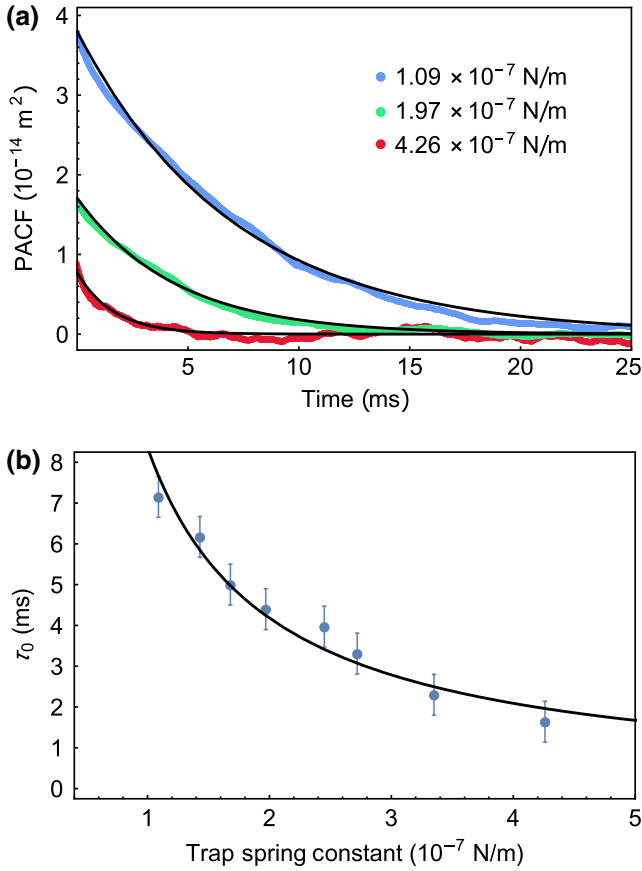
FIG. 5.   (a) PACF of particle motion at various laser powers. The black lines show fits to Eq. (5), based on the overdamped approximation. Part (b) shows the resulting τ_0 from the PACF fits for a range of trap spring constants. The fit function is of the form $\tau_0 = \gamma/\kappa$, from which we obtain $\gamma = (8.38 \pm 0.23) \times 10^{-10}$ kg/s.

mass. The large uncertainty persists even if the values of Γ and κ are constrained on the basis of independent experiments. As a result, we use the autocorrelation function in the large damping limit given by Eq. (5) to fit the data since it has a much simpler functional form. From these fits we extract the correlation time constants with a precision of approximately 3%.

In Fig. 5(b) we show the resulting fit values for the correlation time constant $\tau_0 = \gamma/\kappa$, as a function of trap

spring constant (which is varied by adjusting the laser power). The error bars displayed in this figure represent the total uncertainty due to the intensity filter used to reduce the background noise in the PACFs and the inherent uncertainty in the exponential fits. This data, which exhibits the predicted inverse power dependence, can be used to extract a damping coefficient $\gamma = (8.38 \pm 0.23) \times 10^{-10}$ kg/s. Combining this result with the damping rate Γ measured in the drop experiments, we find a mass value of $(5.55 \pm 0.16) \times 10^{-14}$ kg, which corroborates the determination from the trap restoration experiments discussed earlier (see Table II). If we consider the damping coefficient extracted from Fig. 5(b) and assume Stokes' law, we find the particle radius to be (2.3 ± 0.1) μm, which is comparable to the radius inferred from the images $(2.4 \pm 0.3$ μm). We note that this comparison, which is also shown in Table II, takes into account the effects of calibration uncertainties such as absolute resolution, motional blurring, and depth of field. By combining this radius with the mass, we infer a particle density of $(1.1 \pm 0.1) \times 10^3$ kg/m^3, which is consistent with the density of resins used in common permanent markers [54].

In Fig. 6 we show the MSD constructed from particle positions recorded with a frame rate of 10^5 frames/s. On short timescales, where the motion is expected to transition to the ballistic regime, the MSD disagrees with the prediction based on Eqs. (3) and (6). We attribute this discrepancy to insufficient time resolution, leading to the inability of the MSD to simultaneously fit the behavior on short and long timescales [47]. This aspect is similar to our difficulty in modeling the PACF using Eq. (3), as described earlier in this section. The limitations posed by inadequate time resolution in analyzing such data have been described in Refs. [30] and [55]. Therefore, we use the short timescale behavior of the MSD only as a consistency check for the mass determinations obtained from other techniques (see Table II), all of which rely on particle motion on much longer timescales.

As expected, the data in Fig. 6 deviates from the predictions for the overdamped system [Eqs. (5) and (6)] on short timescales, and approaches the expected trend for ballistic motion [Eqs. (3) and (6)]. We note that this timescale of approximately 100 μs is in agreement with the estimate of the momentum relaxation time made in Sec. II, based on

TABLE II.   Summary of mass and particle radius measurements based on various techniques.

Mass determination		Particle size measurement	
Technique	Mass (kg)	Technique	Radius (μm)
Drop and restore[a]	$(5.58 \pm 0.08) \times 10^{-14}$	Direct observation	2.4 ± 0.3
PACF & drop[b]	$(5.55 \pm 0.16) \times 10^{-14}$	PACF & Stokes[c]	2.3 ± 0.1

[a]Based on 13 measurements conducted with $\kappa = 2.2 \times 10^{-7}$ N/m.
[b]Mass determined by combining τ_0 from Fig. 5(b) and Γ measured in drop experiments [Fig. 3(a)].
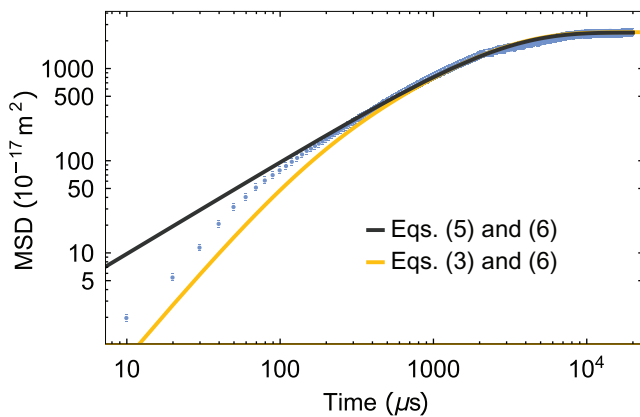[c]Radius measurements inferred from Stokes' law using the PACF time constants from Fig. 5(b).

FIG. 6. MSD for a particle confined in a trap with stiffness $\kappa = 3.2 \times 10^{-7}$ N/m. The black line indicates the MSD predicted by Eqs. (5) and (6) in the overdamped limit. The yellow line indicates the MSD predicted by Eqs. (3) and (6). Both predictions assume that $\gamma = 8.38 \times 10^{-10}$ kg/s and $m = 5.5 \times 10^{-14}$ kg.

assumptions of the particle size and mass (3 μm and 10^{-13} kg, respectively). Using the transition at 100 μs as an upper bound for $\tau_p = m/\gamma$, in combination with the measured particle size (see Table II) and Stokes' law $\gamma = 6\pi r\eta$, we can place a similar bound of $(8.1 \pm 1.3) \times 10^{-14}$ kg on the mass.

This upper bound for τ_p is also consistent with the drop experiments in Fig. 3(a) where $\tau_p = 1/\Gamma = 66$ μs, as well as the estimate ($\tau_p = m/\gamma = 67$ μs) obtained from the combination of the mass from the drop-and-restore experiments (see Table II) and the damping coefficient measured using the PACFs [see Fig. 5(b)].

V. CONCLUSIONS

We present a simple and effective technique based on drop-and-restore experiments in a gravitational field to determine the masses of particles confined using free-space optical tweezers. The mass determination, which has a statistical uncertainty of less than 2%, has also been corroborated by position autocorrelation measurements. In contrast with other techniques (see Table I), our experiments do not require the use of secondary lasers, feedback systems, or vacuum environments. Instead, our measurements rely on direct imaging of scattered light with a fast CMOS sensor and a straightforward spatial calibration procedure.

We anticipate that the precision of this technique can be further improved by using higher laser powers and a larger Rayleigh range for the focused beam. This combination will increase the recapture range, defined by the turning points of the axial intensity gradient and allow the available field of view to be fully exploited. However, potential complications may arise from heating and local changes in the viscosity of the medium, which should be

accounted for at higher laser intensities [35,56,57]. Additionally, we expect that the impulses attributed to the AOM turn on can be significantly suppressed by employing a dual-pass AOM [58]. It is also possible to further reduce the estimated systematic uncertainty by using faster frame rates to improve instantaneous position measurements. Similarly, the accuracy of spring constant measurements can be improved by actively stabilizing the power output of the AOM using an rf feedback loop and by using temperature-insensitive polarizers.

It will be desirable to investigate the widespread applicability of this technique using calibrated microparticles for which the masses and sizes are known. Our drop-and-restore method may also be used to study highly absorbing particles confined in photophoretic traps provided the effects of amplitude modulation in such traps are carefully modeled [36,37]. Other extensions could involve the investigation of particulates trapped in liquids or media of higher viscosity. Based on the statistical precision, we expect that this technique should be applicable to the discrimination of contaminants in flue gases as well as biological agents, such as pollen and pathogens trapped in free space and liquid cultures [11,59–61]. Here, the principal requirement would be the use of an isolated diagnostic chamber to prevent fluid flow. Given the data acquisition time of approximately 90 s, we anticipate that this work will open the door for the rapid determination of relative masses of a variety of trapped particles in future studies.

[1] A. Ashkin and J. M. Dziedzic, Stability of optical levitation by radiation pressure, Appl. Phys. Lett. **24**, 586 (1974).

[2] A. Ashkin and J. M. Dziedzic, Optical levitation of liquid drops by radiation pressure, Science **187**, 1073 (1975).

[3] A. Ashkin and J. M. Dziedzic, Optical levitation in high vacuum, Appl. Phys. Lett. **28**, 333 (1976).

[4] A. Ashkin, Acceleration and Trapping of Particles by Radiation Pressure, Phys. Rev. Lett. **24**, 156 (1970).

[5] A. Ashkin, J. M. Dziedzic, J. E. Bjorkholm, and S. Chu, Observation of a single-beam gradient force optical trap for dielectric particles, Opt. Lett. **11**, 288 (1986).

[6] K. L. Corwin, S. J. M. Kuppens, D. Cho, and C. E. Wieman, Spin-Polarized Atoms in a Circularly Polarized Optical Dipole Trap, Phys. Rev. Lett. **83**, 1311 (1999).

[7] N. Davidson, H. J. Lee, C. S. Adams, M. Kasevich, and S. Chu, Long Atomic Coherence Times in an Optical Dipole Trap, Phys. Rev. Lett. **74,** 1311 (1995).

[8] B. N. Slama-Eliau and G. Raithel, Three-dimensional arrays of submicron particles generated by a four-beam optical lattice, Phys. Rev. E **83,** 051406 (2011).

[9] R. E. Sapiro, B. N. Slama, and G. Raithel, Bragg scattering and Brownian motion dynamics in optically induced crystals of submicron particles, Phys. Rev. E **87,** 052311 (2013).

[10] A. Ashkin, K. Schütze, J. M. Dziedzic, U. Euteneuer, and M. Schliwa, Force generation of organelle transport measured in vivo by an infrared laser trap, Nature **348,** 346 (1990).

[11] A. Ashkin and J. M. Dziedzic, Optical trapping and manipulation of viruses and bacteria, Science **235,** 1517 (1987).

[12] T. T. Perkins, D. E. Smith, R. G. Larson, and S. Chu, Stretching of a single tethered polymer in a uniform flow, Science **268,** 83 (1995).

[13] F. M. Fazal, D. J. Koslover, B. F. Luisi, and S. M. Block, Direct observation of processive exoribonuclease motion using optical tweezers, Proc. Natl. Acad. Sci. **112,** 15101 (2015).

[14] C. Cecconi, E. A. Shank, F. W. Dahlquist, S. Marqusee, and C. Bustamante, Protein-DNA chimeras for single molecule mechanical folding studies with the optical tweezers, Eur. Biophys. J. **37,** 729 (2008).

[15] R. Huang, I. Chavez, K. M. Taute, B. Lukić, S. Jeney, M. G. Raizen, and E.-L. Florin, Direct observation of the full transition from ballistic to diffusive Brownian motion in a liquid, Nat. Phys. **7,** 576 (2011).

[16] T. Li, S. Kheifets, D. Medellin, and M. G. Raizen, Measurement of the instantaneous velocity of a Brownian particle, Science **328,** 1673 (2010).

[17] T. Li and M. G. Raizen, Brownian motion at short time scales, Ann. Phys. **525,** 281 (2013).

[18] B. Lukić, S. Jeney, Ž. Sviben, A. J. Kulik, E.-L. Florin, and L. Forró, Motion of a colloidal particle in an optical trap, Phys. Rev. E **76,** 011112 (2007).

[19] B. Lukić, S. Jeney, C. Tischer, A. J. Kulik, L. Forró, and E.-L. Florin, Direct Observation of Nondiffusive Motion of a Brownian Particle, Phys. Rev. Lett. **95,** 160601 (2005).

[20] D. R. Burnham, P. J. Reece, and D. McGloin, Parameter exploration of optically trapped liquid aerosols, Phys. Rev. E **82,** 051123 (2010).

[21] R. Di Leonardo, G. Ruocco, J. Leach, M. J. Padgett, A. J. Wright, J. M. Girkin, D. R. Burnham, and D. McGloin, Parametric Resonance of Optically Trapped Aerosols, Phys. Rev. Lett. **99,** 010601 (2007).

[22] N. B. Viana, M. S. Rocha, O. N. Mesquita, A. Mazolli, P. A. Maia Neto, and H. M. Nussenzveig, Towards absolute calibration of optical tweezers, Phys. Rev. E **75,** 021914 (2007).

[23] T. Franosch, M. Grimm, M. Belushkin, F. M. Mor, G. Foffi, L. Forró, and S. Jeney, Resonances arising from hydrodynamic memory in Brownian motion, Nature **478,** 85 (2011).

[24] E. Hebestreit, M. Frimmer, R. Reimann, and L. Novotny, Sensing Static Forces with Free-Falling Nanoparticles, Phys. Rev. Lett. **121,** 063602 (2018).

[25] C. Guzmán, H. Flyvbjerg, R. Köszali, C. Ecoffet, L. Forró, and S. Jeney, In situ viscometry by optical trapping interferometry, Appl. Phys. Lett. **93,** 184102 (2008).

[26] M. Grimm, T. Franosch, and S. Jeney, High-resolution detection of Brownian motion for quantitative optical tweezers experiments, Phys. Rev. E **86,** 021912 (2012).

[27] P. Purohit, A. Samadi, P. M. Bendix, J. J. Laserna, and L. B. Oddershede, Optical trapping reveals differences in dielectric and optical properties of copper nanoparticles compared to their oxides and ferrites, Sci. Rep. **10,** 1 (2020).

[28] I. Chavez, R. Huang, K. Henderson, E.-L. Florin, and M. G. Raizen, Development of a fast position-sensitive laser beam detector, Rev. Sci. Instrum. **79,** 105104 (2008).

[29] J. P. Staforelli, E. Vera, J. M. Brito, P. Solano, S. Torres, and C. Saavedra, Superresolution imaging in optical tweezers using high-speed cameras, Opt. Express **18,** 3322 (2010).

[30] K. Berg-Sørensen and H. Flyvbjerg, Power spectrum analysis for optical tweezers, Rev. Sci. Instrum. **75,** 594 (2004).

[31] K. Berg-Sørensen, E. J. G. Peterman, T. Weber, C. F. Schmidt, and H. Flyvbjerg, Power spectrum analysis for optical tweezers. II: Laser wavelength dependence of parasitic filtering, and how to achieve high bandwidth, Rev. Sci. Instrum. **77,** 063106 (2006).

[32] F. Ricci, M. T. Cuairan, G. P. Conangla, A. W. Schell, and R. Quidant, Accurate mass measurement of a levitated nanomechanical resonator for precision force-sensing, Nano Lett. **19,** 6711 (2019).

[33] C. P. Blakemore, A. D. Rider, S. Roy, A. Fieguth, A. Kawasaki, N. Priel, and G. Gratta, Precision Mass and Density Measurement of Individual Optically Levitated Microspheres, Phys. Rev. Appl. **12,** 024037 (2019).

[34] J. Liu and K.-D. Zhu, Highly sensitive mass detection using optically levitated microdisks, IEEE Sens. J. **19,** 7269 (2019).

[35] G.-H. Chen, L. He, M.-Y. Wu, and Y.-Q. Li, Temporal Dependence of Photophoretic Force Optically Induced on Absorbing Airborne Particles by a Power-Modulated Laser, Phys. Rev. Appl. **10,** 054027 (2018).

[36] S. K. Bera, A. Kumar, S. Sil, T. K. Saha, T. Saha, and A. Banerjee, Simultaneous measurement of mass and rotation of trapped absorbing particles in air, Opt. Lett. **41,** 4356 (2016).

[37] J. Lin, J. Deng, R. Wei, Y.-Q. Li, and Y. Wang, Measurement of mass by optical forced oscillation of absorbing particles trapped in air, J. Opt. Soc. Am. B **34,** 1242 (2017).

[38] J. Blum, S. Bruns, D. Rademacher, A. Voss, B. Willenberg, and M. Krause, Measurement of the Translational and Rotational Brownian Motion of Individual Particles in a Rarefied Gas, Phys. Rev. Lett. **97,** 230601 (2006).

[39] G. Carlse, A. Pouliot, T. Vacheresse, A. Carew, H. C. Beica, S. Winter, and A. Kumarakrishnan, Technique for magnetic moment reconstruction of laser-cooled atoms using direct imaging and prospects for measuring magnetic sublevel distributions, J. Opt. Soc. Am. B **37,** 1419 (2020).

[40] P. Langevin, Sur la théorie du mouvement Brownien, Comptes Rendus **146,** 530 (1908).

[41] G. E. Uhlenbeck and L. S. Ornstein, On the theory of the Brownian motion, Phys. Rev. **36,** 823 (1930).

[42] M. C. Wang and G. E. Uhlenbeck, On the theory of the Brownian motion II, Rev. Mod. Phys. **17**, 323 (1945).

[43] R. B. Bird, W. E. Stewart, and E. N. Lightfoot, *Transport Phenomena* (John Wiley and Sons Inc., New York, NY, USA, 2007), 2nd ed.

[44] L. Gilchrist, An absolute determination of the viscosity of air, Phys. Rev. **1**, 124 (1913).

[45] S. Velasco, On the Brownian motion of a harmonically bound particle and the theory of a Wiener process, Eur. J. Phys. **6**, 259 (1985).

[46] F. Reif, *Fundamentals of Statistical and Thermal Physics* (Waveland Press, Long Grove, IL, USA, 2009).

[47] G. Carlse, M.S. Thesis, York University, 2020.

[48] H. C. Beica, A. Pouliot, A. Carew, A. Vorozcovs, N. Afkhami-Jeddi, G. Carlse, P. Dowling, B. Barron, and A. Kumarakrishnan, Characterization and applications of auto-locked vacuum-sealed diode lasers for precision metrology, Rev. Sci. Instrum. **90**, 085113 (2019).

[49] A. Pouliot, H. C. Beica, A. Carew, A. Vorozcovs, G. Carlse, and A. Kumarakrishnan, in *High-Power Diode Laser Technology XVI* (International Society for Optics and Photonics, San Francisco, CA, USA, 2018), Vol. 10514, p. 105140S.

[50] T. Polster, S. Leopold, and M. Hoffmann, in *Smart Sensors, Actuators, and MEMS V* (International Society for Optics and Photonics, Prague, Czech Republic, 2011), Vol. **8066**, p. 80661F.

[51] M. Esseling, P. Rose, C. Alpmann, and C. Denz, Photophoretic trampoline–interaction of single airborne absorbing droplets with light, Appl. Phys. Lett. **101**, 131115 (2012).

[52] K. C. Neuman and S. M. Block, Optical trapping, Rev. Sci. Instrum. **75**, 2787 (2004).

[53] J. Bechhoefer and S. Wilson, Faster, cheaper, safer optical tweezers for the undergraduate laboratory, Am. J. Phys. **70**, 393 (2002).

[54] I. D. van der Werf, G. Germinario, F. Palmisano, and L. Sabbatini, Characterisation of permanent markers by pyrolysis gas chromatography–mass spectrometry, Anal. Bioanal. Chem. **399**, 3483 (2011).

[55] H. Flyvbjerg and H. G. Petersen, Error estimates on averages of correlated data, J. Chem. Phys. **91**, 461 (1998).

[56] E. J. G. Peterman, F. Gittes, and C. F. Schmidt, Laser-induced heating in optical traps, Biophys. J. **84**, 1308 (2003).

[57] D. McGloin, D. R. Burnham, M. D. Summers, D. Rudd, N. Dewar, and S. Anand, Optical manipulation of airborne particles: Techniques and applications, Faraday Discuss. **137**, 335 (2008).

[58] G. Spirou, I. Yavin, M. Weel, A. Vorozcovs, A. Kumarakrishnan, P. Battle, and R. Swanson, A high-speed-modulated retro-reflector for lasers using an acousto-optic modulator, Can. J. Phys. **81**, 625 (2003).

[59] Y. Pang, H. Song, J. H. Kim, X. Hou, and W. Cheng, Optical trapping of individual human immunodeficiency viruses in culture fluid reveals heterogeneity with single-molecule resolution, Nat. Nanotechnol. **9**, 624 (2014).

[60] J. Lin, A. G. Hart, and Y.-Q. Li, Optical pulling of airborne absorbing particles and smut spores over a meter-scale distance with negative photophoretic force, Appl. Phys. Lett. **106**, 171906 (2015).

[61] Z. Zhang, T. E. P. Kimkes, and M. Heinemann, Manipulating rod-shaped bacteria with optical tweezers, Sci. Rep. **9**, 1 (2019).